crystals

MDPI

Article

Efficient Adsorption Removal of Tetrabromobisphenol A from Water by Using a Magnetic Composite Fe_3O_4/GO/ZIF-67

Sumei Li [1,2,*], Jian Ji [2], Saisai Shan [1,2,3], Sha Chen [1,2], Hanbing Li [1,2], Qian Xu [1,2] and Yixuan Liang [1,2]

[1] Department of Environment, Faculty of Environment and Life, Beijing University of Technology, Beijing 100124, China; chensha@bjut.edu.cn (S.C.); hanbingli@bjut.edu.cn (H.L.)
[2] Key Laboratory of Beijing on Regional Air Pollution Control, Faculty of Environment and Life, Beijing University of Technology, Beijing 100124, China
[3] Zhongjiayuan (Beijing) Testing Certification, Beijing 100124, China
* Correspondence: sumei_li@bjut.edu.cn

Abstract: Tetrabromobisphenol A (TBBPA) is a kind of widely used brominated flame retardant (BFR), which is proven to be harmful to ecological systems and public health. It is very important to remove TBBPA from the environment. In our study, a magnetic composite named Fe_3O_4/GO/ZIF-67 was synthesized by a coprecipitation method and applied in the highly efficient adsorption of TBBPA from water. Static adsorption experiments demonstrated that the adsorption capacity could reach 232 $mg\cdot g^{-1}$ within 120 min, which is much higher than those reported in the other literature. The experimental results show that the adsorption of TBBPA on Fe_3O_4/GO/ZIF-67 followed Langmuir and pseudo-second-order kinetic adsorption models. The main mechanisms for these adsorptions were identified as hydrogen bonds between OH groups in TBBPA and COOHs of Fe_3O_4/GO/ZIF-67, and π-π stacking between Fe_3O_4/GO/ZIF-67 and TBBPA. This study provides a method with great promise for the design and synthesis of better adsorbents for the removal of TBBPA from the water environment.

Keywords: TBBPA; metal–organic frameworks; adsorption; magnetic separation; Fe_3O_4/GO/ZIF-67

check for updates

Citation: Li, S.; Ji, J.; Shan, S.; Chen, S.; Li, H.; Xu, Q.; Liang, Y. Efficient Adsorption Removal of Tetrabromobisphenol A from Water by Using a Magnetic Composite Fe_3O_4/GO/ZIF-67. *Crystals* **2024**, *14*, 508. https://doi.org/10.3390/cryst14060508

Academic Editor: Philippe Trens

Received: 29 April 2024
Revised: 16 May 2024
Accepted: 23 May 2024
Published: 27 May 2024

1. Introduction

Brominated flame retardants (BFRs) are widely used in numerous aspects of human life for plastics, textiles, electronics, and etc. Tetrabromobisphenol A (TBBPA) is one kind of intensively used BFR with a large level of production in plastics, electronics, and textiles, used to improve their fire safety [1]. The global annual consumption of TBBPA ranges between 120,000 and 150,000 tons. Notably, Asia exhibits the highest consumption rate, with an annual figure reaching 89,400 tons [2]. As an additive flame retardant, TBBPA has characteristics of continuous biomagnification and endocrine-disrupting effects [3,4]. TBBPA also has numerous bad effects on biota and mankind, such as nephrotoxicity, immunotoxicity, endocrine-disrupting effects, hepatotoxicity, and neurotoxicity [5]. Except for dust [6], water [7], air [8], soil [9], sediment [10], and sewage sludge [11], TBBPA has also been found in animals [12,13], and even in blood [14] and breast milk [15] from humans. Negative impacts associated with TBBPA exposure, including nephrotoxicity, immunotoxicity, endocrine disruption, hepatotoxicity, and neurotoxicity, have been observed in both animal models and human studies [16]. Therefore, it is urgent to develop fast techniques of high efficiency to remove TBBPA from the aquatic environment.

Varieties of methods for removing TBBPA from the environment include light radiation [17], microbial degradation [18], oxidative degradation [19], adsorption [20], and so on [21]. However, the light radiation method is costly, the microbial method is unstable, and the oxidative degradation method involves the risk of secondary pollution. Among them, adsorption removal is regarded as an effective method for eliminating TBBPA from water due to its high efficiency, simple operational process, and economy [22]. Hence, it is of great significance to design and synthesize materials with functional porosity that can effectively adsorb and remove TBBPA from water.

Recently, a highly porous group of materials, known as metal–organic frameworks (MOFs), have attracted the interest of researchers and rapidly become a research focus in material, chemistry, and environmental sciences [23]. However, a single MOF is seldom used for the adsorption of TBBPA, and combining it with other functional materials to improve their performance is a more common method. Li et al. synthesized polyoxometalate-modified Cu-BTC MOFs, which exhibited notably higher attraction to TBBPA [24]. The maximum adsorption capacity of this material was about 3.65 $mg \cdot g^{-1}$, and the removal rate of TBBPA reached up to 95%. Zhou et al. introduced magnetic nanoparticles into a zeolite imidazole skeleton-67 to prepare a carbon nanotube@zeolite imidazole skeleton-67 (CNTs@ZIF-67) [25]. This material showed both magnetic separation and adsorption capacities, with an adsorption capacity of TBBPA of 92.1 $mg \cdot g^{-1}$. Zhou et al. fabricated a surface molecular-imprinted polymer Fe_3O_4@ZIF-8@MIP and used it to selectively adsorb TBBPA from water, and the maximum value of its adsorption capacity was about 118 $mg \cdot g^{-1}$ [26]. However, the adsorption capacity of TBBPA was still not high enough, and needs to be improved to enable better water treatment.

To further improve the adsorption capacity and optimize the practical applications of MOFs, we prepared a magnetic MOF composite Fe_3O_4/GO/ZIF-67 via a coprecipitation method. Magnetic MOF composites showed easy and convenient separation and recovery properties. Furthermore, the behavior and mechanism of the composite regarding TBBPA adsorption were studied, and the influencing factors of pH, adsorption time, adsorption capacity, and initial concentrations of TBBPA were explored. Besides this, the adsorption characteristics, including adsorption kinetics and adsorption isotherms, were studied. The possible adsorption mechanism was also assessed.

2. Materials and Methods

2.1. Chemicals and Reagents

Cobalt nitrate hexahydrate was obtained from Tianjin Xiensi Biochemical Technology Co. Ltd. (Tianjin, China); Dimethyl imidazole was given by Shanghai Aladdin Biochemical Technology Co. Ltd. (Shanghai, China); Methanol was purchased from Thermo Fisher Scientific Co. Ltd. (Shanghai, China); Absolute ethanol was purchased from Tianjin Damao chemical reagent factory (Tianjin, China); Anhydrous sodium acetate, trisodium citrate dihydrate, thioglycolic acid (TGA), and graphene oxide were purchased from Shanghai McLean Biochemical Technology Co., Ltd. (Shanghai, China); Both HCl and NaOH were obtained from Tianjin Guangfu Technology Development Co., Ltd. (Tianjin, China); TBBPA (99% purity, CAS: 79-94-7) was purchased from Afaesha Chemical Co., Ltd. (Shanghai, China).

2.2. Experimental Instruments

The physical structures of the samples were analyzed with the aid of SEM (ZEISS Gemini 300) (Zeiss, Tokyo, Japan) at an accelerating voltage of 2.0 kv. Magnetic hysteresis curves were acquired by a vibrating sample magnetometer (VSM, LakeShore 7404) (LakeShore, Carson, CA, USA) at room temperature. N_2 adsorption–desorption isotherms were obtained at a temperature of 76 K using liquid nitrogen, and the specific surface areas of the samples were determined by use of the Brunauer–Emmett–Teller equation (BET, MicromeriticsASAP2010M) (Anton Paar, Torrance, CA, USA) method. The crystal structures of samples were tested by X-ray powder diffraction (XRD, Smartlab 3) (Rigaku, Tokyo, Japan). Fourier Transform infrared spectroscopy (FT-IR, IRAffinity-1) (Shimadzu, Kyoto, Japan) was used to determine the structures and changes of some special functional groups in the sample. The zeta potential was determined by a zeta potential analyzer (SD-UPT-10) (BioLogic, Göttingen, German). High-performance liquid chromatography (HPLC, Agilent 1260 Infinity) (Agilent, Santa Clara, CA, USA) was applied to measure the concentrations of TBBPA. The raw data were obtained by plotting in Origin 2022.

2.3. Preparation of Magnetic Material Fe_3O_4/GO

Fe_3O_4 particles were synthesized via the solvothermal method; 1.0 mmol of $FeCl_3 \cdot 6H_2O$ powder, 1.4 mmol of trisodium citrate dihydrate and 29.3 mmol of anhydrous sodium acetate were accurately weighed with an analytical balance and then dissolved in 60 mL of ethylene glycol. After being fully stirred with a magnetic stirrer for 30 min, 4.2 mmol of GO was added to the mixture. These were transferred to a polytetrafluoroethylene-lined high-pressure reactor and heated in an oven at 200 °C for 12 h, then a magnetic material (Fe_3O_4/GO) was obtained. After cooling and separating, Fe_3O_4/GO was washed with deionized water and absolute ethanol three times, and then dried in a constant-temperature drying oven at 60 °C.

2.4. Preparation of Fe_3O_4/GO/ZIF-67

Here, 2.0 mmol of cobalt nitrate hexahydrate was dissolved in methanol (30 mL), with the addition of 0.1 mmol of Fe_3O_4/GO, and then stirred for 1 h. Then, 12.0 mmol of dimethyl imidazole was dissolved in another methanol solution (10 mL). Then, dimethyl imidazole solution was added to the cobalt salt solution slowly, with vigorous stirring. After mixing evenly, it was left at room temperature for 24 h and centrifuged. After washing with ethanol several times, it was dried in an oven at 60 °C to obtain the Fe_3O_4/GO/ZIF-67 composite. The synthetic method of ZIF-67 was the same as above, except that no Fe_3O_4/GO was added during the reaction.

2.5. Adsorption Performance of Fe_3O_4/GO/ZIF-67

Here, 10 mg of Fe_3O_4/GO/ZIF-67 was added into a series of different concentrations of TBBPA methanol/water solution (2:3, V:V) (ranging from 5 to 200 $mg \cdot L^{-1}$) at 100 mL. The temperature and the rate of the shaker were controlled at 298.15 K and 120 rmp for 2 h, respectively. After magnetic separation, the concentrations of TBBPA in the supernatant were detected by an HLPC. Each test was performed in triplicate.

The adsorption kinetics were also studied in order to study the relationship between the adsorption quantity and time. Here, 20 mg of Fe_3O_4/GO/ZIF-67 was added into 100 mL of methanol/water (2:3, v:v) solution containing 20 $mg \cdot L^{-1}$ of TBBPA. After incubation at 298.15 K for different durations, the supernatant was magnetically separated and then subjected to HPLC to determine TBBPA. The equilibrium adsorption quantity of TBBPA can be calculated by the following formula:

$$Q_t = \frac{(C_0 - C_t)V}{m} \tag{1}$$

C_t (mg L^{-1}) is the TBBPA concentration at different times.

3. Results and Discussion

3.1. Synthesis of Fe_3O_4/GO/ZIF-67

We prepared a magnetic MOF composite (Fe_3O_4/GO/ZIF-67) via the coprecipitation method (see Figure 1). This is due to the fact that GO, a derivative of graphene produced by deep oxidation, has a large specific surface area and a lot of π-π binding sites, which can efficiently adsorb TBBPA molecules. The oxidized graphene oxide carries many oxygen-containing functional groups on its surface, such as -COOH and -OH, which can directly adsorb or bond with TBBPA molecules (Figure 1). The magnetic material Fe_3O_4/GO was fabricated via a solvothermal method, and they were covered with ZIF-67 to obtain Fe_3O_4/GO/ZIF-67. The reaction yield of this chemical synthesis process was about 86.3%.

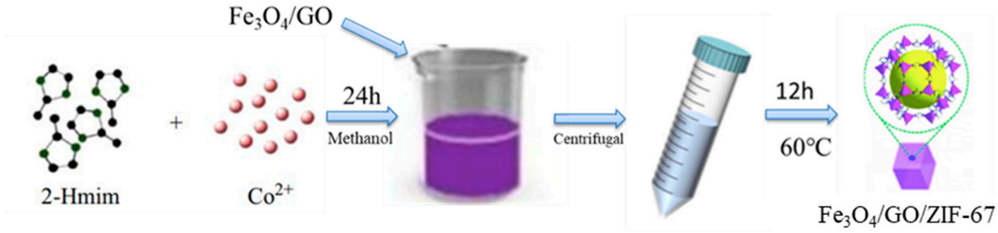

Figure 1. Scheme of preparation of magnetic MOF composites.

3.2. Characterization

The crystal structures of Fe_3O_4/GO, ZIF-67, and Fe_3O_4/GO/ZIF-67 nanoparticles were characterized by XRD and are shown in Figure 2a. The s series of diffraction peaks of Fe_3O_4/GO displayed at 2θ = 31.5°, 35.6°, 43.3°, 53.7°, 57.1°, 62.7°, and 74.5° correspond to (220), (311), (400), (422), (511), (440) and (622) planes, which are in good agreement with the standard XRD cards (JCPDS, PDF,75-0033). A series of diffraction peaks of ZIF67 was seen at 2θ = 7.39°, 10.36°, 12.79°, 14.71°, 16.45°, 18.01°, 22.19°, 24.64°, and 26.72°, corresponding to the (011), (002), (112), (022), (013), (222), (114), (233) and (134) planes. In the magnetic composites, the characteristic peaks of ZIF-67 were retained, revealing that the doping of Fe_3O_4/GO did not affect the crystal structure of ZIF-67.

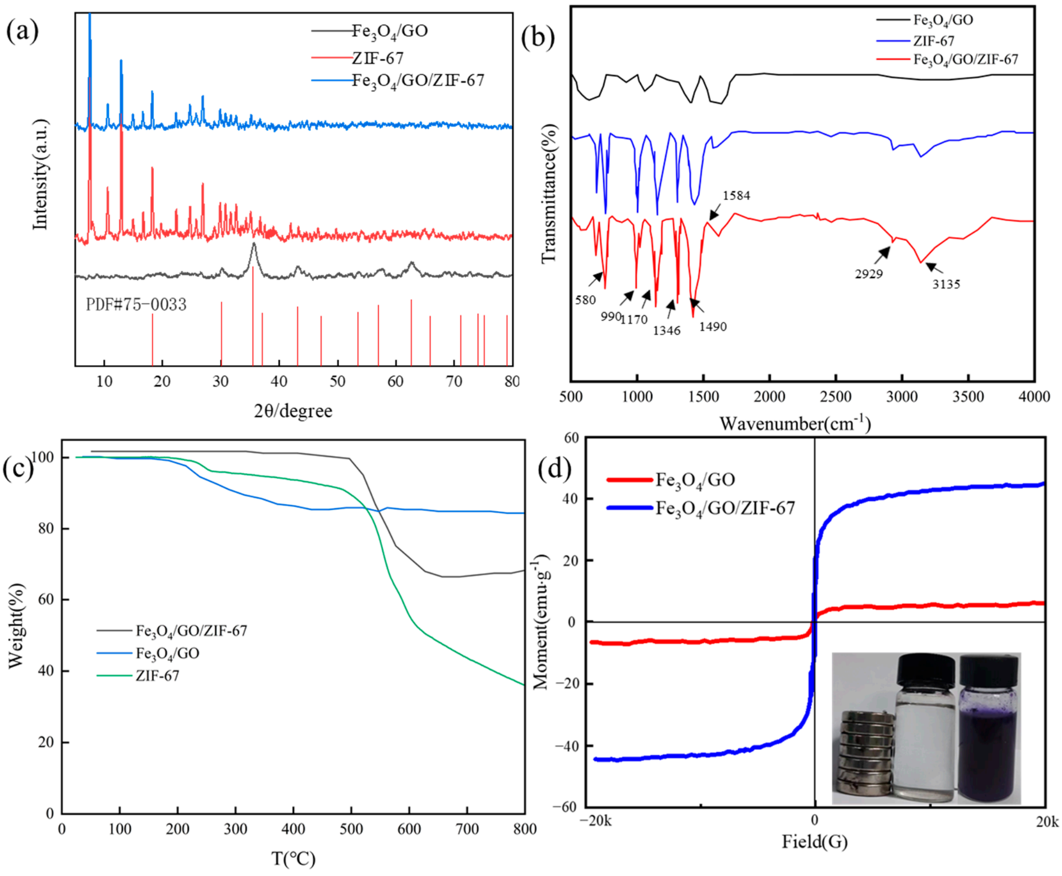

Figure 2. XRD patterns of Fe_3O_4/GO, ZIF-67 and Fe_3O_4/GO/ZIF-67 (**a**). Infrared spectra of Fe_3O_4/GO, ZIF-67 and Fe_3O_4/GO/ZIF-67 (**b**). TGA analysis of Fe_3O_4/GO, ZIF-67 and Fe_3O_4/GO/ZIF-67 (**c**). Magnetic hysteresis loops of Fe_3O_4/GO and Fe_3O_4/GO/ZIF-67 (**d**).

Functional group analyses of materials were performed using FT-IR spectra (see Figure 2b). The absorption peak at 580 cm^{-1} in Fe_3O_4 corresponded to the stretching vibration of the Fe–O bond. Meanwhile, the peak of ZIF-67 mainly came from its ligand dimethyl imidazole. Two characteristic peaks of ZIF-67 and Fe_3O_4/GO were found in

Fe_3O_4/GO/ZIF-67, indicating that Fe_3O_4/GO was successfully embedded in the synthesis of ZIF-67.

The TGA curve of the prepared sample is shown in Figure 2c. There was only a 10% weight loss for ZIF-67 alone at around 500 °C, which was because of the elimination of guest molecules and unreacted substances. When the temperature reached 800 °C, the structure of MOF began to collapse. Therefore, ZIF-67 is thermally stable at temperatures up to 500 °C, which exceeds this value for most MOF materials. When the temperature reached 400 °C, the mass loss rate of Fe_3O_4/GO material was about 12%, and then when the temperature rose to 800 °C, the material showed no mass loss. This indicates that Fe_3O_4/GO has high thermal stability and temperature resistance. After forming the composite, the stability of the MOF material was enhanced. When the temperature reached 600 °C, the mass loss rate was about 29%, indicating that the incorporation of Fe_3O_4/GO improved the stability of the MOF material.

The magnetic characteristics of Fe_3O_4/GO and Fe_3O_4/GO/ZIF-67 were examined using a VSM 25 °C in a magnetic field ranging from −20 to +20 kOe. The hysteresis loops are depicted in Figure 2d. The saturation magnetizations of the two specimens were 44.1 and 6.2 $emu \cdot g^{-1}$, respectively, indicating their suitability for separation from the solution under an external magnetic field. These findings demonstrate that Fe_3O_4/GO/ZIF-67 could be swiftly retrieved from the reaction system within mere seconds.

The morphology and structure of Fe_3O_4/GO, ZIF-67, and Fe_3O_4/GO/ZIF-67 were characterized by SEM. In Figure 3a, the morphology of Fe_3O_4/GO is labeled; Fe_3O_4 takes the shape of a nanosphere and GO takes the shape of sheets. In addition, the nanospherical shape of the magnetic particles facilitates better binding and the homogeneous distribution of other materials during synthesis [27,28]. Figure 3d shows that the average size of ZIF-67 was about 500 nm, and it had a rhombic dodecahedral structure, with a side length of around 200 nm. Figure 3c,d shows that Fe_3O_4 was successfully embedded in the surface of ZIF-67.

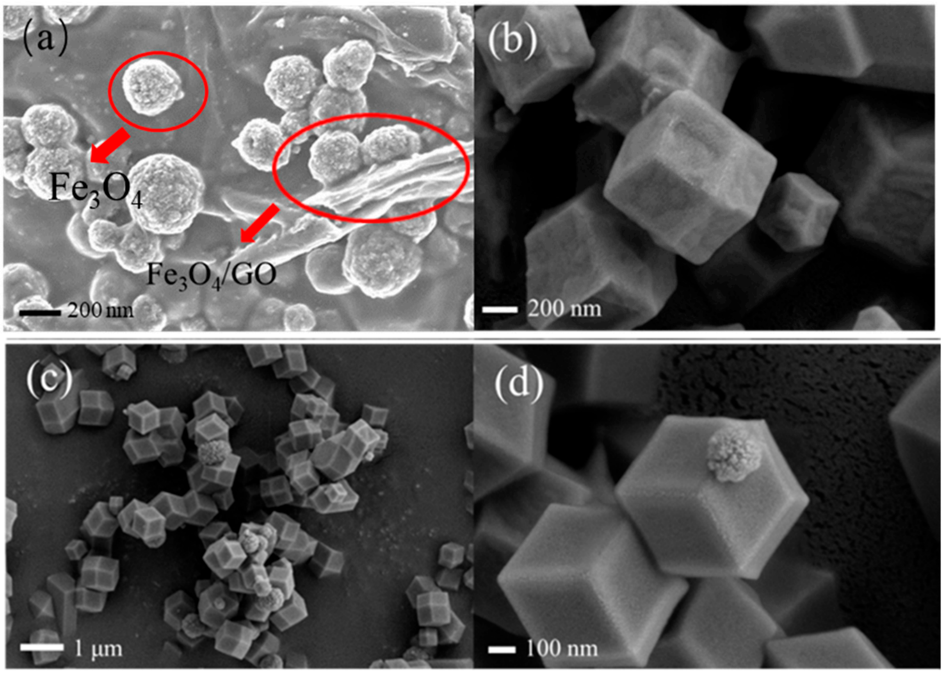

Figure 3. SEM images of Fe_3O_4/GO (**a**), ZIF-67 (**b**) and Fe_3O_4/GO/ZIF-67 (**c**,**d**).

The specific surface area (S_a) and pore volume (V_p) of Fe_3O_4/GO, ZIF-67 and Fe_3O_4/GO/ZIF-67 were determined via a nitrogen adsorption–desorption experiment, as illustrated in Figure 4. The S_a of ZIF-67 and Fe_3O_4/GO/ZIF-67 were 2196 and 1912 $m^2 \cdot g^{-1}$, respectively. The results of the BJH method show that the V_p and pore diameter of ZIF-67 were 0.72 $cm^3 \cdot g^{-1}$ and 1.32 nm, respectively, while those of Fe_3O_4/GO/ZIF-67 were

0.63 $cm^3 \cdot g^{-1}$ and 1.31 nm, respectively. From the data, we can infer that the decrease in S_a was possibly due to the Fe_3O_4 that was evenly dispersed on the of ZIF-67 surface and covering the crystals. Table 1 shows the pore structure parameters and specific surface area of ZIF-67 and Fe_3O_4/GO/ZIF-67. It could be seen that the N_2-saturated adsorption capacity of Fe_3O_4/GO/ZIF-67 decreased after Fe_3O_4/GO modification. This indicates that the S_a of Fe_3O_4/GO/ZIF-67 was lower than the original ZIF-67. This may be because the Fe_3O_4/GO introduced occupied part of the surface and pores of ZIF-67. Figure 4 shows that the pores in ZIF-67 and Fe_3O_4/GO/ZIF-67 were micropores.

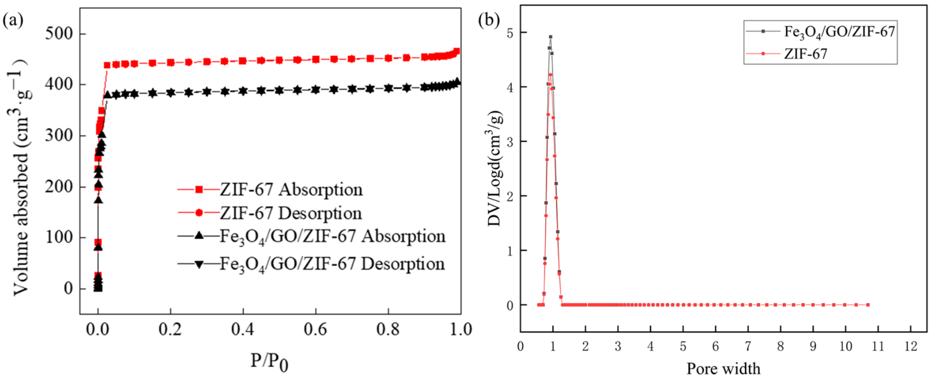

Figure 4. N_2 adsorption–desorption isotherms of ZIF-67 and Fe_3O_4/GO/ZIF-67 (**a**) and pore size distribution of Fe_3O_4/GO/ZIF-67 (**b**).

Table 1. Specific surface area and pore structure parameters of ZIF-67 and Fe_3O_4/GO/ZIF-67.

Adsorbent	Specific Surface Area ($m^2 \cdot g^{-1}$)	Hole Capacity ($cm^3 \cdot g^{-1}$)	Aperture (nm)
ZIF-67	2196	0.72	1.32
Fe_3O_4/GO/ZIF-67	1912	0.63	1.31

3.3. Factors Affecting the Adsorption of TBBPA by Fe_3O_4/GO/ZIF-67

3.3.1. Effects of pH and Ionic Strengths

Figure 5a,b shows the effects of Fe_3O_4/GO/ZIF-67 on the adsorption capacity of TBBPA at different pH values. The first-order and second-order dissociation constants of TBBPA were 7.5 and 8.5, respectively. When the pH values of the solution were greater than the pK_a of TBBPA, TBBPA was mainly present in the form of anions. When the pH values were less than the pK_a of TBBPA, TBBPA was mainly present as cation.

In order to explore the influence of electrostatic force in the adsorption process, the zeta potential was analyzed. According to the zeta potential diagram (Figure 5b), while the pH = 2, the adsorption capacity was 0. This is probably because the material structure was damaged under highly acidic conditions. When the pH was between 3 and 4, the material surface was positively charged and mutually exclusive with TBBPA in the form of cations. When the pH was between 4 and 7, the material's surface was negatively charged and attracted TBBPA, and the adsorption capacity of TBBPA was able to reach its highest value. When the pH was above 7, TBBPA was present in the form of anions, which repelled the negatively charged material surface, resulting in a decrease in the adsorption capacity. Thus, pH 6 was selected as the optimal pH value in the following experiments.

The variety of ions in the real water environment could affect the adsorption capacity of Fe_3O_4/GO/ZIF-67 in relation to TBBPA. Cl^-, SO_4^{2-}, CO_3^{2-}, HCO^{3-}, Na^+, K^+, and Ca^{2+} are among the ions that were chosen in order to study the use of Fe_3O_4/GO/ZIF-67 in complicated water environments. The variations in the capacity of Fe_3O_4/GO/ZIF-67 to absorb TBBPA in the presence of external ions were quite small, as Figure 5c illustrates. Consequently, the adsorption of TBBPA by Fe_3O_4/GO/ZIF-67 is not greatly influenced by these ions in the water environment.

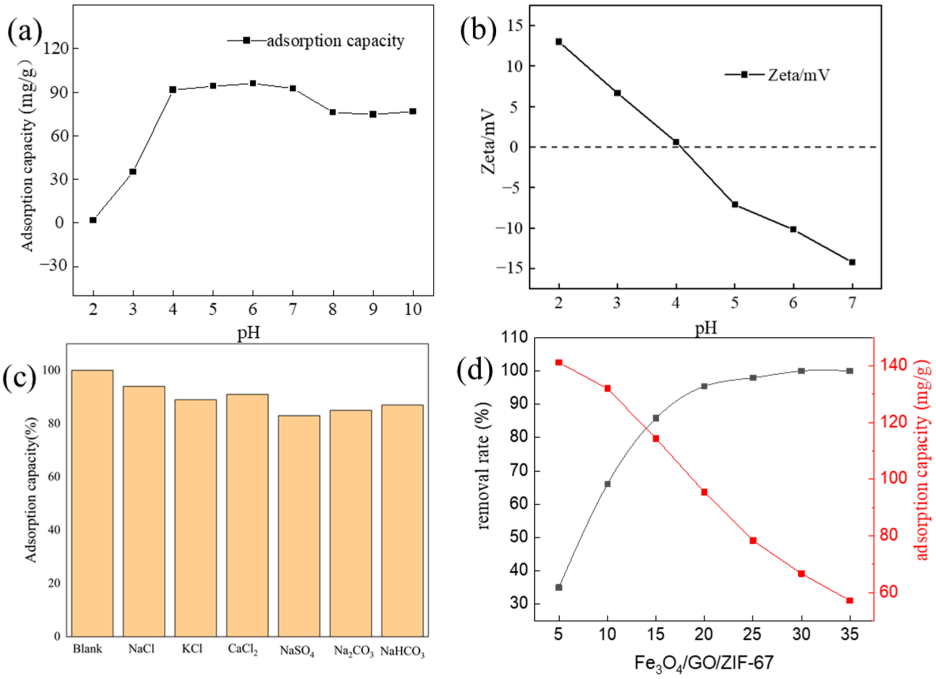

Figure 5. Effect of solution pH on TBBPA adsorption (**a**) (SD: ±7.31%); zeta potentials of adsorption (**b**) (SD: ±9.11%); effect of interfering ions on adsorption (**c**) (C_0 = 10 mg L^{-1}, m = 10 mg, pH = 6, *t* = 120 min) (SD: ±5.07%) and effect of Fe_3O_4/GO/ZIF-67 dosage (**d**) (SD: ±5.46%).

3.3.2. Effects of Adsorbent Dosage

Figure 5d shows the effects of the dosage of Fe_3O_4/GO/ZIF-67 on the adsorption capacity, and the removal rates of TBBPA. With the increase in Fe_3O_4/GO/ZIF-67 dosage, the removal rate of TBBPA gradually increased. When the dosage was increased to 20 mg, the adsorption removal rate of TBBPA reached about 95.4%. With the continuously increasing dosage of Fe_3O_4/GO/ZIF-67, the removal rate of TBBPA changed little, and the unit adsorption capacity gradually decreased. Therefore, the optimal dosage of Fe_3O_4/GO/ZIF-67 was 20 mg.

3.4. Kinetic Adsorption and Isotherms

3.4.1. Adsorption Kinetics

Figure 6 shows the TBBPA adsorption kinetics curve of Fe_3O_4/GO/ZIF-67 at 298.15 K. After 3 min, Q_T was able to reach 70.1 mg·g^{-1}, which was 73.5% of the equilibrium adsorption capacity. The binding amount exhibited a gradual increase and eventually reached equilibrium after 120 min. The active sites on Fe_3O_4/GO/ZIF-67 were conducive to the binding and removal of TBBPA. These well-arranged channels and the substantial specific surface area of MOFs facilitated the rapid adsorption.

In the kinetic study on the adsorption of TBBPA by Fe_3O_4/GO/ZIF-67, the adsorption process of TBBPA was studied through the pseudo-first-order kinetic model (Formula (2)) and the pseudo-second-order kinetic model (Formula (3)).

$$\ln(q_e - q_t) = lnq_e - k_1 t \tag{2}$$

$$\frac{t}{q_t} = \frac{1}{k_2 q_e^2} + \frac{t}{q_e} \tag{3}$$

where *t* (min) is the adsorption time; q_e (mg·g^{-1}) is the adsorption amount at moment of equilibrium; q_t (mg·g^{-1}) is the adsorption capacity at *t* time; k_1 (min^{-1}) and k_2 (g·mg^{-1}·min^{-1}) are pseudo-first-order kinetic adsorption constants and pseudo-second-order kinetic adsorption constants, respectively.

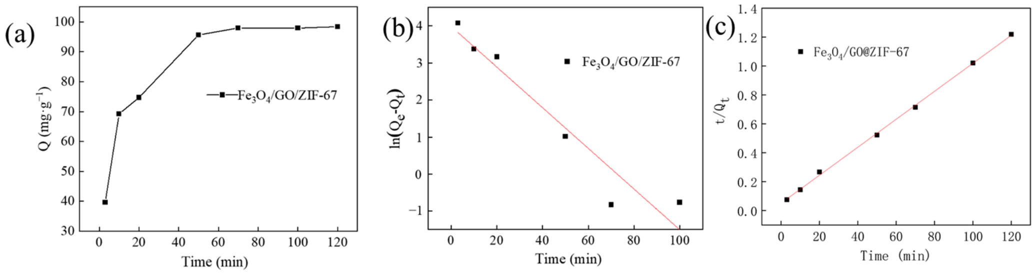

Figure 6. (**a**) Effect of time on adsorption capacity (C_0 = 10 mg L^{-1}, m = 10 mg, pH = 6, t = 120 min) (SD: ±6.34%). (**b**) Pseudo-first-order kinetic model, and (**c**) pseudo-second-order kinetic model.

To delve deeper into the adsorption dynamics of TBBPA on Fe_3O_4/GO/ZIF-67, simulations were conducted to analyze both the pseudo-first-order and the pseudo-second-order kinetics of the adsorption process. As shown in Figure 6, according to the fitting parameters in Table 2, the linear correlation coefficient R^2 of the pseudo-second-order kinetic model for the process of adsorption of TBBPA by Fe_3O_4/GO/ZIF-67 was 0.999, which is greater than the correlation coefficient of the first-order kinetic model of 0.910, and the quantity of theoretical equilibrium adsorption obtained via public calculation is 98.4 mg·g^{-1}, which is close to the value in the experimental data of 95.4 mg·g^{-1}, indicating that the kinetics of adsorption of TBBPA onto Fe_3O_4/GO/ZIF-67 followed the pseudo-second-order model more closely. The main step taken to control the reaction rate was the chemical adsorption process. The surface of the adsorbent Fe_3O_4/GO/ZIF-67 contained a significant number of adsorption sites, which can be bonded with pollutants through chemical bonds.

Table 2. Adsorption kinetic parameters.

C_{TBBPA} (mg·L^{-1})	q_{exp} (mg·g^{-1})	Model	Rate Constant	q_e (mg·g^{-1})	R^2
20	98.39	Pseudo-first-order dynamic model	K_1 (min^{-1}) 0.0549	63.4	0.910
		Pseudo-second-order dynamic model	K_2 (g·mg^{-1}·min^{-1}) 0.0018	103	0.999

3.4.2. Adsorption Isotherm Study

Here, 100 mL of TBBPA solution was prepared at the concentrations of 5, 10, 20, 40, 60, 80, 100, 120, 150, and 200 mg·L^{-1} in a solution with volume ratios of methanol to water of 2:3 and 3:2, respectively, and in the pure methanol solution. Here, 0.02 g of Fe_3O_4/GO/ZIF-67 was added into a 150 mL conical flask with TBBPA solution at 25 °C, with a rotation speed of 120 rpm, for 120 min. Then, a magnet was used to adsorb the material on the bottom of the conical flask, and the supernatant was taken out with a syringe. The concentrations of TBBPA in the remaining solution were determined with an HPLC. The adsorption capacity was calculated, and the capacity of Fe_3O_4/GO/ZIF-67 to absorb TBBPA in methanol aqueous solutions with different pollutant concentrations and volume ratios was obtained.

As shown in Figure 7a, with the increase in the initial concentrations of TBBPA, the adsorption capacity gradually increased. When the concentration exceeded 160 mg·L^{-1}, the trend of increase in the adsorption capacity was small. When the concentration was 200 mg·L^{-1}, the adsorption capacity of TBBPA was the largest. At the same time, the influence of the volume ratio of methanol to water on the adsorption of TBBPA was investigated. With increases in the volume ratio of methanol to water, TBBPA was made easily soluble in methanol, and was not easily adsorbed by the adsorbent, meaning the adsorption capacity gradually decreased. When the ratio of methanol to water was 2:3, the adsorption capacity was the largest, reaching up to 232 mg·g^{-1}. Figure 8 summarizes the adsorption capacity when TBBPA was adsorbed by many kinds of materials. It can be seen that Fe_3O_4/GO/ZIF-67 acted as an excellent adsorbent material to TBBPA.

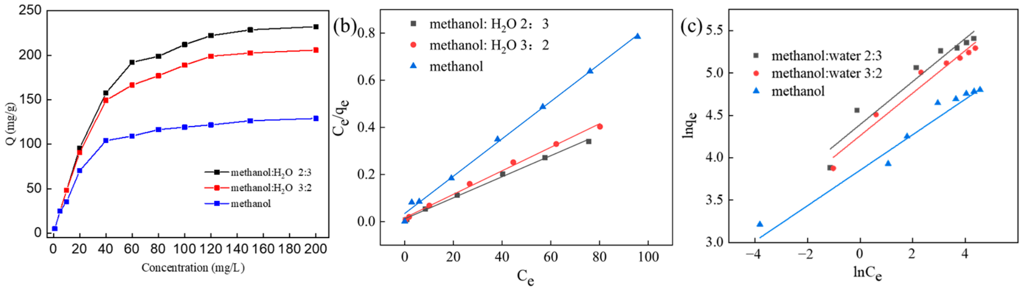

Figure 7. (**a**) Effect of initial concentrations of TBBPA on adsorption capacity (C_0 = 10 mg L^{-1}, m = 10 mg, pH = 6, t = 120 min) (SD: ±3.16%). (**b**) Langmuir adsorption model and (**c**) Freundlich adsorption model.

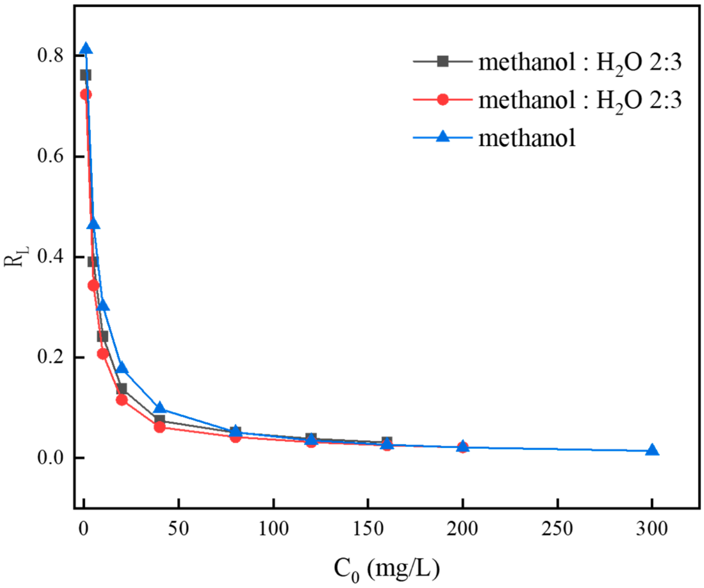

Figure 8. Separation factor R_L shown by Fe_3O_4/GO/ZIF-67 composite.

Adsorption isotherms are commonly employed to characterize the partitioning of adsorbate species between liquid and solid phases in the academic literature. Figure 7 shows the TBBPA adsorption isotherms of Fe_3O_4/GO/ZIF-67 in different solvents at 298.15 K. At the initial stage, the adsorption capacity of TBBPA increased greatly and then increased slowly with the increasing concentration of TBBPA, until saturation. The capacity of Fe_3O_4/GO/ZIF-67 to adsorb TBBPA, q_e, in a methanol and water mixture (2:3) reached 232 mg·g^{-1}, surpassing that of Fe_3O_4@ZIF-8@MIP (118 mg·g^{-1}) and other materials. This demonstrates the superior performance of Fe_3O_4/GO/ZIF-67 in comparison to alternative adsorbents [29]. This material's high adsorption capacity as regards TBBPA can be ascribed to its large specific surface area (see Table 3). Here, K_L is Langmuir constant (L/mg) and C_0 is the initial concentration of DB80 solution 23 (mg·L^{-1}).

Table 3. Comparison of the adsorption capacity of Fe_3O_4/GO/ZIF-67 with those of other materials.

Adsorbent	q_{max} **(mg·g^{-1})**	**Ref.**
PWA@Cu-BTC	3.65	[30]
Fe_3O_4@ZIF-8 Fe_3O_4@ZIF-8@MIP	81.00 117.60	[31]
MCNT@ZIF-67	83.23	[25]
GO	115.77	[7]
Fe_3O_4/GO/ZIF-67	232.00	This paper

The adsorption isotherms of TBBPA on Fe_3O_4/GO/ZIF-67 were studied. The experimental data were analyzed by Langmuir (Formula (4)) and Freundlich (Formula (5)).

$$\frac{C_e}{q_e} = \frac{C_e}{q_{max}} + \frac{1}{q_{max}K_L} \tag{4}$$

$$\ln q_e = \frac{1}{n} lnC_e + lnK_F \tag{5}$$

C_e represents the equilibrium mass concentration ($mg \cdot L^{-1}$); q_e denotes the adsorption capacity of the adsorbent at equilibrium ($mg \cdot g^{-1}$); q_{max} stands for the maximum adsorption capacity of Fe_3O_4/GO/ZIF-67 ($mg \cdot g^{-1}$); K_L and K_F represent the adsorption rate constants for the Langmuir and Freundlich models, respectively. The dimensionless equilibrium separation factor, R_L, is a crucial characteristic of the Langmuir isotherm and can be expressed as the following equation:

$$R_L = \frac{1}{1 + K_L C_0} \tag{6}$$

A value of R_L equal to zero indicates an irreversible type of isotherm. Conversely, an R_L value falling between 0 and 1 suggests a favorable adsorption behavior. However, when R_L exceeds 1, the adsorption process is deemed unfavorable. Figure 8 shows R_L values in the range of 0.01–0.81, revealing that the adsorption behavior is favorable.

The adsorption isotherm model of Fe_3O_4/GO/ZIF-67 for TBBPA was studied under different methanol–water volume ratios. Figure 7 shows the linear diagrams of (C_e/q_e) for C_E and the lnq_e for lnc_e of the Langmuir and Freundlich models, respectively; the parameters of the Langmuir and Freundlich models are summarized in Table 4. The correlation coefficient obtained by the Langmuir model was higher than that obtained by the Freundlich model. The results show that the adsorption of TBBPA on Fe_3O_4/GO/ZIF-67 was more suitable under the Langmuir model, indicating that the adsorption of TBBPA on Fe_3O_4/GO/ZIF-67 suggested monolayer adsorption, and the adsorption binding sites on the adsorbent surface were uniform.

Table 4. Adsorption isotherm constants of the Fe_3O_4/GO/ZIF-67.

Solvents	q_{exp} **($mg \cdot g^{-1}$)**	**Model**	**Parameter 1**	**Parameter 2**	**R^2**
Methanol–water 2:3 Methanol–water 3:2 Pure methanol	222.15 198.97 121.8	Langmuir model	q_{max} ($mg \cdot g^{-1}$)	K_L ($L \cdot mg^{-1}$)	
			224	0.3827	0.9963
			200	0.3129	0.9949
			126	0.2309	0.9961
		Freundlich model	K_F ($mg \cdot g^{-1}$)/($mg \cdot L^{-1}$)$^{-n}$	n	
			80.9	3.94	0.9200
			70.9	3.99	0.9528
			47.2	4.78	0.8587

3.5. Possible Adsorption Mechanism

The adsorption processes of organic pollutants often entail intricate host–guest interactions. Typically, coordination interactions occur between the metal sites of the adsorbent and the organic groups of TBBPA. It can be seen from Table 1 that the adsorbent Fe_3O_4/GO/ZIF-67 has a microporous structure, thus TBBPA cannot enter the pores of the adsorbent, because the kinetic diameter of TBBPA (10.8 × 7.2 Å) is larger than the pore size of Fe_3O_4/GO/ZIF-67 (1.31 Å). Therefore, we hypothesize that the adsorption of TBBPA predominantly took place at the surface of Fe_3O_4/GO/ZIF-67.

In addition, the specific surface area of Fe_3O_4/GO/ZIF-67 is relatively high (1912 $m^2 \cdot g^{-1}$), providing rich active sites for the adsorption of TBBPA. Among them, there is an interaction between the COOH bonds of Fe_3O_4/GO/ZIF-67 and TBBPA. The COOH bond in Fe_3O_4/GO/ZIF-6 promotes the formation of hydrogen bonds with the hydroxyl group of TBBPA, facilitating a favorable interaction [31]. The interaction between the benzene ring of Fe_3O_4/GO/ZIF-67 and the benzene ring of TBBPA favors the formation of a π-π interaction. Combined with the influence of the molecular structure and pH value of TBBPA, we speculate that there were two mechanisms involved in the process of the adsorption of TBBPA by Fe_3O_4/GO/ZIF-67, including hydrogen bonding between the OH group in TBBPA and the COOH in Fe_3O_4/GO/ZIF-67, and π-π stacking between the adsorbent and pollutant, as shown in Figure 9.

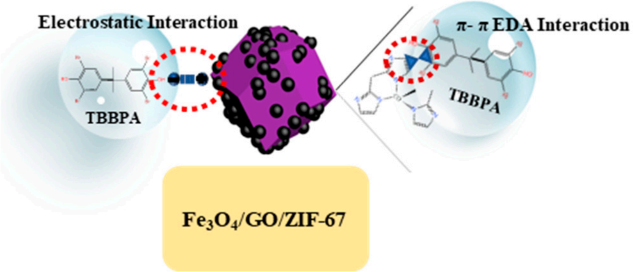

Figure 9. Proposed mechanism of chemisorption of TBBPA by Fe_3O_4/GO/ZIF-67.

4. Conclusions

We designed and synthesized a magnetic composite Fe_3O_4/GO/ZIF-67 and used it in the adsorptive removal of TBBPA. The addition of a carboxyl group greatly improves the hydrophilicity of Fe_3O_4/GO/ZIF-67 and ensures it has good dispersibility. Taking ZIF-67 as the skeleton greatly improves the specific surface area of the material and the adsorption efficiency of TBBPA. Under the interaction of hydrogen bonds and π-π stacking, the maximum TBBPA-adsorption capacity of the material was 232 $mg \cdot g^{-1}$, which is much higher than those of other MOF-related materials. Fe_3O_4/GO/ZIF-67 has fast adsorption kinetics, a large adsorption capacity and environmental adaptability, and so it has high applicability in the removal of TBBPA from water. This study shows the prospect of applying reasonably designed magnetic composite MOFs materials in the adsorption and removal of TBBPA from water. In the future, we will continue to improve the stability of this MOF-related material and explore its application in a real water environment.

Author Contributions: Conceptualization, S.L.; methodology, J.J. and S.S.; software, J.J., Q.X. and S.S.; validation, S.L., Y.L., H.L. and S.C.; formal analysis, S.L., J.J. and S.S.; investigation, S.S.; resources, Y.L.; data curation, S.S., Q.X. and S.L.; writing—original draft preparation, J.J. and S.S.; writing—review and editing, S.L.; visualization, J.J. and S.S.; supervision, S.L. and S.C.; project administration, S.L.; funding acquisition, H.L. All authors have read and agreed to the published version of the manuscript.

Funding: This research was funded by the R&D Program of Beijing Municipal Education Commission, grant number KM202310005018.

Data Availability Statement: The raw data supporting the conclusions of this article will be made available by the authors on request.

Conflicts of Interest: The authors declare no conflicts of interest.

References

1. de Wit, C.A.; Alaee, M.; Muir, D.C.G. Levels and Trends of Brominated Flame Retardants in the Arctic. *Chemosphere* **2006**, *64*, 209–233. [CrossRef] [PubMed]
2. Liu, K.; Li, J.; Yan, S.; Zhang, W.; Li, Y.; Han, D. A Review of Status of Tetrabromobisphenol A (TBBPA) in China. *Chemosphere* **2016**, *148*, 8–20. [CrossRef] [PubMed]

3. Rosal, R.; Rodríguez, A.; Perdigón-Melón, J.A.; Petre, A.; García-Calvo, E.; Gómez, M.J.; Agüera, A.; Fernández-Alba, A.R. Occurrence of Emerging Pollutants in Urban Wastewater and Their Removal through Biological Treatment Followed by Ozonation. *Water Res.* **2010**, *44*, 578–588. [CrossRef] [PubMed]
4. Oberg, O.; Warman, K. Distribution and Levels of Brominated Flame Retardants in Sewage Sludge. *Chemosphere* **2002**, *48*, 805–809. [CrossRef] [PubMed]
5. Labadie, P.; Tlili, K.; Alliot, F.; Bourges, C.; Desportes, A.; Chevreuil, M. Development of Analytical Procedures for Trace-Level Determination of Polybrominated Diphenyl Ethers and Tetrabromobisphenol A in River Water and Sediment. *Anal. Bioanal. Chem.* **2010**, *396*, 865–875. [CrossRef] [PubMed]
6. Harrad, S.; Abdallah, M.A.E.; Rose, N.L.; Turner, S.D.; Davidson, T.A. Current-Use Brominated Flame Retardants in Water, Sediment, and Fish from English Lakes. *Environ. Sci. Technol.* **2009**, *43*, 9077–9083. [CrossRef]
7. Zhang, Y.; Zhou, S.; Su, X.; Xu, J.; Nie, G.; Zhang, Y.; He, Y.; Yu, S. Synthesis and Characterization of Ag-Loaded p-Type TiO_2 for Adsorption and Photocatalytic Degradation of Tetrabromobisphenol A. *Water Environ. Res.* **2020**, *92*, 713–721. [CrossRef] [PubMed]
8. Gu, H.; Lou, H.; Tian, J.; Liu, S.; Tang, Y. Reproducible Magnetic Carbon Nanocomposites Derived from Polystyrene with Superior Tetrabromobisphenol A Adsorption Performance. *J. Mater. Chem. A Mater.* **2016**, *4*, 10174–10185. [CrossRef]
9. Peng, H.; Pan, B.; Wu, M.; Liu, R.; Zhang, D.; Wu, D.; Xing, B. Adsorption of Ofloxacin on Carbon Nanotubes: Solubility, PH and Cosolvent Effects. *J. Hazard. Mater.* **2012**, *211–212*, 342–348. [CrossRef]
10. Fang, L.; Xu, L.; Li, J.; Huang, L.Z. Copper Nanoparticles/Graphene Modified Green Rusts for Debromination of Tetrabromobisphenol A: Enhanced Galvanic Effect, Electron Transfer and Adsorption. *Sci. Total Environ.* **2019**, *683*, 275–283. [CrossRef]
11. Ji, L.; Bai, X.; Zhou, L.; Shi, H.; Chen, W.; Hua, Z. One-Pot Preparation of Graphene Oxide Magnetic Nanocomposites for the Removal of Tetrabromobisphenol A. *Front. Environ. Sci. Eng.* **2013**, *7*, 442–450. [CrossRef]
12. Zhang, B.; Zhang, L.; Akiyama, K.; Bingham, P.A.; Zhou, Y.; Kubuki, S. Self-Assembly of Nanosheet-Supported Fe-MOF Heterocrystals as a Reusable Catalyst for Boosting Advanced Oxidation Performance via Radical and Nonradical Pathways. *ACS Appl. Mater. Interfaces* **2021**, *13*, 22694–22707. [CrossRef]
13. Gnanasekaran, G.; Arthanareeswaran, G.; Mok, Y.S. A High-Flux Metal-Organic Framework Membrane (PSF/MIL-100 (Fe)) for the Removal of Microplastics Adsorbing Dye Contaminants from Textile Wastewater. *Sep. Purif. Technol.* **2021**, *277*, 119655. [CrossRef]
14. Liang, Y.; Zhang, Q.; Li, S.; Fei, J.; Zhou, J.; Shan, S.; Li, Z.; Li, H.; Chen, S. Highly Efficient Removal of Quinolones by Using the Easily Reusable MOF Derived-Carbon. *J. Hazard. Mater.* **2022**, *423*, 127181. [CrossRef]
15. Zhou, T.; Zhao, X.; Xu, Y.; Tao, Y.; Luo, D.; Hu, L.; Jing, T.; Zhou, Y.; Wang, P.; Mei, S. Electrochemical Determination of Tetrabromobisphenol A in Water Samples Based on a Carbon Nanotubes@zeolitic Imidazole Framework-67 Modified Electrode. *RSC Adv.* **2020**, *10*, 2123–2132. [CrossRef]
16. Xie, L.; Liu, D.; Huang, H.; Yang, Q.; Zhong, C. Efficient Capture of Nitrobenzene from Waste Water Using Metal-Organic Frameworks. *Chem. Eng. J.* **2014**, *246*, 142–149. [CrossRef]
17. Yang, S.; Hai, F.I.; Nghiem, L.D.; Nguyen, L.N.; Roddick, F.; Price, W.E. Removal of Bisphenol A and Diclofenac by a Novel Fungal Membrane Bioreactor Operated under Non-Sterile Conditions. *Int. Biodeterior. Biodegrad.* **2013**, *85*, 483–490. [CrossRef]
18. Saint-Louis, R.; Pelletier, E. LC-ESI-MS-MS Method for the Analysis of Tetrabromobisphenol A in Sediment and Sewage Sludge. *Analyst* **2004**, *129*, 724–730. [CrossRef]
19. Ji, Y.; Kong, D.; Lu, J.; Jin, H.; Kang, F.; Yin, X.; Zhou, Q. Cobalt Catalyzed Peroxymonosulfate Oxidation of Tetrabromobisphenol A: Kinetics, Reaction Pathways, and Formation of Brominated by-Products. *J. Hazard. Mater.* **2016**, *313*, 229–237. [CrossRef]
20. Li, L.; Liu, X.L.; Geng, H.Y.; Hu, B.; Song, G.W.; Xu, Z.S. A MOF/Graphite Oxide Hybrid (MOF: HKUST-1) Material for the Adsorption of Methylene Blue from Aqueous Solution. *J. Mater. Chem. A Mater.* **2013**, *1*, 10292–10299. [CrossRef]
21. Jun, B.M.; Hwang, H.S.; Heo, J.; Han, J.; Jang, M.; Sohn, J.; Park, C.M.; Yoon, Y. Removal of Selected Endocrine-Disrupting Compounds Using Al-Based Metal Organic Framework: Performance and Mechanism of Competitive Adsorption. *J. Ind. Eng. Chem.* **2019**, *79*, 345–352. [CrossRef]
22. Watanabe, I.; Kashimoto, T.; Tatsukawa, R. *Identification of the Flame Retardant TetrabromobisphenoI-A in the River Sediment and the Mussel Collected in Osaka*; Springer-Verlag New York Inc.: New York, NY, USA, 1983; Volume 31.
23. De Wit, C.A.; Sverige. Naturvårdsverket. In *Brominated Flame Retardants*; Swedish Environmental Protection Agency (Naturvårdsverket): Stockholm, Sweden, 2000; ISBN 9162050656.
24. Minna, L.; Sun, P.; Wu, Q.; Liu, D.; Zhou, L. Core-Shell Magnetic Metal-Organic Framework Molecularly Imprinted Nanospheres for Specific Adsorption of Tetrabromobisphenol A from Water. *Environ. Sci. Nano* **2018**, *5*, 2651–2662.
25. Zhou, T.; Tao, Y.; Xu, Y.; Luo, D.; Hu, L.; Feng, J.; Jing, T.; Zhou, Y.; Mei, S. Facile Preparation of Magnetic Carbon Nanotubes@ZIF-67 for Rapid Removal of Tetrabromobisphenol A from Water Sample. *Environ. Sci. Pollut. Res.* **2018**, *25*, 35602–35613. [CrossRef]
26. Zhou, T.; Feng, Y.; Zhou, L.; Tao, Y.; Luo, D.; Jing, T.; Shen, X.; Zhou, Y.; Mei, S. Selective and Sensitive Detection of Tetrabromobisphenol-A in Water Samples by Molecularly Imprinted Electrochemical Sensor. *Sens. Actuators B Chem.* **2016**, *236*, 153–162. [CrossRef]
27. Marcuello, C.; Chambel, L.; Rodrigues, M.S.; Ferreira, L.P.; Cruz, M.M. Magnetotactic Bacteria: Magnetism Beyond Magnetosomes. *IEEE Trans. Nanobiosci.* **2018**, *17*, 555–559. [CrossRef] [PubMed]

28. Wang, Q.; Ma, X.; Liao, H.; Liang, Z.; Li, F.; Tian, J.; Ling, D. Artificially Engineered Cubic Iron Oxide Nanoparticles as a High-Performance Magnetic Particle Imaging Tracer for Stem Cell Tracking. *ACS Nano* **2020**, *14*, 2053–2062. [CrossRef] [PubMed]
29. Zheng, J.; Lin, Z.; Lin, G.; Yang, H.; Zhang, L. Preparation of Magnetic Metal-Organic Framework Nanocomposites for Highly Specific Separation of Histidine-Rich Proteins. *J. Mater. Chem. B* **2015**, *3*, 2185–2191. [CrossRef]
30. Li, X.; Pillai, S.C.; Wei, L.; Liu, Z.; Huang, L.; Huang, Q.; Jia, X.; Hou, D.; Song, H.; Wang, H. Facile Synthesis of Polyoxometalate-Modified Metal Organic Frameworks for Eliminating Tetrabromobisphenol-A from Water. *J. Hazard. Mater.* **2020**, *399*, 122946. [CrossRef]
31. Lastovina, T.A.; Budnyk, A.P. A Review of Methods for Extraction, Removal, and Stimulated Degradation of Microplastics. *J. Water Process Eng.* **2021**, *43*, 102209. [CrossRef]